Hindawi
Adsorption Science & Technology
Volume 2022, Article ID 5061627, 10 pages
https://doi.org/10.1155/2022/5061627

Research Article

Petrology and Tectonic Geophysics of Massive and Foliated Eclogites in the North Qilian Orogenic Belt: Changes in Mineral Composition, Oxygen Fugacity, and Fabric during Exhumation

Feng Wang,[1] **Daorong Zhou**,[2] **and Xunhua Zhang**[3]

[1]*College of Earth Sciences, Jilin University, Changchun, Jilin 130061, China*
[2]*Nanjing Geological Survey Center, Nanjing, Jiangsu 210016, China*
[3]*Qingdao Institute of Marine Geology, Qingdao, Shandong 266071, China*

Correspondence should be addressed to Feng Wang; fwang15@mails.jlu.edu.cn

Received 16 July 2022; Revised 30 July 2022; Accepted 1 August 2022; Published 23 September 2022

Academic Editor: Rabia Rehman

The North Qilian orogenic belt is a typical area of "cold" subduction of the early Paleozoic oceanic plate, forming a series of high pressure and low temperature metamorphic rock assemblages. Among them, eclogite is a kind of protolith, which is basaltic or gabbro high pressure metamorphic rock, mainly composed of garnet and chlorite which are two kinds of minerals. Eclogites record the entire history of subduction zone metamorphism and later exhumation. Due to the crystal habit and the developed joints, the strength of the pyroxene in the matrix is weak, so it is subjected to the main strain during deformation, whereas garnet tends to show only passive rotational deformation. This paper presents some new results in petrology and tectonic geophysics of eclogite block-like and planar eclogite. The massive and facial eclogite rocks contain eclogite facies mineral assemblages, and the peak temperature and pressure conditions are $t = 450 \sim 520^{\circ}C$ and $P = 1.9 \sim 2.3$ GPa, which are consistent with the adjacent eclogite. Combined with the characteristics of in situ Lu-Hf isotopes, Ce^{4+}/Ce^{3+} ratios of zircons, relative oxygen fugacity, and absolute oxygen fugacity, it is shown that the oxygen fugacity of the granodiorite porphyry (BL023, BLO31, DB048) of the folio chemical and massive eclogite deposits are all located in MH (magnetite-hematite) buffer zone. Through the calculation results of absolute oxygen fugacity of rock mass, it can be seen that the absolute oxygen fugacity of ore-bearing rock mass is significantly higher than that of non-ore-bearing rock mass. This paper systematically summarizes the research progress of the microscopic and ultrastructural deformation of eclogite minerals in high-pressure metamorphic zones, and discusses the changes of mineral composition, oxygen fugidity, and fabric of eclogite deformation characteristics during the recovery of subduction and reentry.

1. Introduction

Orogenic belt is a narrow and strong tectonic deformation zone caused by the violent tectonic change of the lithosphere and the reconstruction of its material and structure in the upper part of the earth, resulting in the compression and contraction of the crust. It often forms linear relatively uplifted mountains on the surface. There are banded tectonic belts with certain orogenic polarity on the earth. Orogenic belts are distributed on the edge of plates, between plates, or within plates. The orogenic belt has strong tectonic deformation and concentrated hydrothermal activity. It is a very important place to study the composition, structure, deformation, and geodynamics of the crust or lithosphere. The study of continental lithosphere has become an important frontier of modern geoscience, and orogenic belt has always been one of the most attractive research topics in continental tectonics. There are mainly three types of orogenic belts: noncollisional orogenic belts, collisional orogenic belts, and intracontinental orogenic belts, such as the North American Cordillera orogen and the Andean-type orogen).The North Qilian Mountains orogenic belt is a typical accretionary orogenic belt [1]. It is located in the northeastern margin of the Qinghai-Tibet Plateau and distributes

in a NW direction. It is an important part of the Central Orogenic Belt in China [2]. It consists of multiple lithological tectonic units of different origins and ages, including subducted slab sediments, submarine accretionary complexes, island arc igneous rocks, submarine plateaus, oceanic islands, Precambrian continental crustal remnants, ophiolite rock fragments, and basin clastic sedimentary rocks [3]. The North Qilian orogenic belt is a product formed by the subduction, accretion, and splicing of the ancient Qilian Ocean. Because of its unique geological tectonic background and long and complex geological evolution history, it has always been the focus and hotspot of scholars at home and abroad [4]. The Qilian orogenic belt is located in the hinterland of China, with convenient transportation and unique natural conditions. It is an ideal natural laboratory for the study of orogenic belt, ophiolite mantle rock and mantle rock deformation, lithospheric layered interaction and crust mantle interaction, paleomantle plume structure, and geodynamics.

In recent years, most scholars have carried out systematic research on the Paleozoic magmatic rocks, metamorphic rocks, and sedimentary rocks in the area by means of geochemistry, detrital zircon chronology, and tectonic dynamics mechanism and have achieved many results [5]. There are mainly two ophiolites in the North Qilian, the Biandukou, Dachadaban and Jiujiequan ophiolite melange belts in the north belt, and the Dongcaohe, Yushigou and Aoyougou ophiolite mixed belts in the south rock belt [6]. The northern belt is the remnant of the back-arc basin formed by the northward subduction of the Neoproterozoic-Early Paleozoic ancient Qilian Ocean, and the southern belt is the remnant of the Neoproterozoic-Early Paleozoic ancient Qilian oceanic crust [7]. At present, a relatively unified understanding of the tectonic evolution history of the ancient Qilian Ocean has been obtained, which is mainly divided into four stages, namely, the Cambrian North Qilian Ocean subduction southward, the Early-Middle Ordovician North Qilian Ocean subduction northward, and the late cocollision period [8]. The Ordovician and the late orogeny of the early Silurian and the middle and late Silurian came to an end [9]. The North Qilian orogenic belt contains metamorphic rocks such as massive and foliated eclogites [10]. Among them, the ultra-high pressure and high-pressure metamorphic minerals such as garnet, omphacite, polysilicon muscovite, and even coesite in the eclogite record in the history of high-pressure and ultra-high pressure metamorphism experienced by the crustal rocks, and the zircon in the eclogite also records the original eclogite [11].

2. Materials and Methods

Different scholars have different views on the tectonic evolution of the Qilian orogenic belt and its geophysical mechanism [12]. In the 1970s, Jiqing explained the tectonic evolution of the Qilian orogenic belt with the view of cyclic trough structure. Xuchang et al. first discovered the ophiolite belt in the North Qilian orogenic belt, thus confirming the existence of the Early Paleozoic oceanic crust in the North Qilian area, and laying a foundation for putting forward the theory of plate tectonics in the Qilian area. Lindi et al. sorted out the tectonic evolution of the North Qilian area on the basis of previous studies and believed that the North Qilian area experienced the formation of oceans, the formation of oceanic basins from the Proterozoic to the Devonian subduction, the formation of arc-ditch basin systems, the extinction of oceans, and the process of collisional orogeny [13]. Sun et al. proposed a multistage subduction and collision geodynamic model based on the metamorphic deformation characteristics of metamorphic rocks in the Qilian orogenic belt [14]. Lee and Jung proposed a two-way subduction model of the North Qilian Ocean in the late twentieth century. However, there are still different understandings on the tectonic properties or attribution of the continental crustal remnants in the North Qilian Mountains [13].

The rupture and convergence of supercontinents have an important impact on global sea level rise and fall, climate change, and the formation of mineral resources, and are a major plate tectonic event in geological history [15]. Research in recent years has shown that at least two large-scale, global supercontinent convergence and disintegration events occurred in Columbia and Rodinia during the Proterozoic [16]. In the study of orogenic belts, Yu et al. found that in addition to Neoproterozoic orogenic belts, older orogenic belts were widely developed in the ancient craton margins at 2.1-1.8 Ga, and these ancient orogenic belts were widely developed. The orogenic belt not only exists on the edge of one craton, but is widely distributed on different cratons around the world. Based on this discovery, the Columbia supercontinent was proposed and became a research hotspot of the supercontinent [17]. Supercontinent is the combination of almost all continental blocks on the earth. The formation of supercontinents is closely related to the horizontal movement of continental blocks in the process of geological history, that is, the "birth" of plates restricts the formation of supercontinents. However, there are different understandings about when the plate was "born" in geological history. In the early stage, it was believed that the plate mechanism was only applicable to the Mesozoic, and then gradually extended to the end of Mesoproterozoic and even the end of Paleoproterozoic. The main reason was that there was no ophiolite suite, a remnant of Phanerozoic oceanic crust, found in the early Earth history.

The Beidahe Group is the oldest Precambrian microcontinent remaining in the North Qilian orogenic belt, and it is an important carrier for the study of the Precambrian tectonic evolution in the North Qilian area [18]. The research on its tectonic dynamic background is very weak and there are many controversies. Zhang et al. and Feng et al. discovered bimodal volcanic rocks in this area and believed that the original rocks of the Beidahe Group were formed in an intracontinental rift environment. However, Gao and Fu et al. believed that the Beidahe rock group was formed in the continental margin arc environment, which was formed by the subduction and accretion of the ancient ocean between the Paleoproterozoic North China Craton and the Qaidam Craton [19].

In recent years, there have been many studies on eclogites in the North Qilian orogenic belt, and people have made great progress in many aspects around the reentry

behavior and mechanism of ultra-high pressure metamorphic rocks, such as petrology and mineralogy. Peak metamorphic conditions and P-T-t evolution trajectories of various ultra-high pressure metamorphic rocks. Combined with geochemical characteristics, it is deduced that the protoliths of most eclogites are Late Proterozoic base-type and acidic magmatic rocks [20]. The discovery of abnormally low-oxygen isotope and carbon isotope values indicates that most of the original rocks of ultra-high pressure metamorphic rocks had undergone strong water-rock exchange with cold atmospheric precipitation before subduction; fluid inclusions and minerals such as rare earth and trace elements [21]. It shows that during the reentry process, the ultra-high pressure metamorphic rocks maintained a relatively closed state, and no large-scale dispersive fluid inflow and outflow activities occurred; in addition, the existence of various fluid inclusions and veins, eclogite [22]. The heterogeneity of retrograde metamorphism, the discovery of potassium feldspar+quartz±plagioclase inclusions in eclogite, the discovery of molten structure, etc., all indicate that structural water precipitation occurred in the process of ultra-high pressure metamorphic rock and formed a local area [23]. Fluid reaction and partial melting of decompression; in terms of structure, the combination of CCSD deep drilling cores and regional outcrops allows people to more accurately understand the structural framework of the entire ultra-high pressure metamorphic body from a three-dimensional space, and the deep crust of the drilling holes can also be identified [24]. Ductile shear zones that can be mapped to regions; the widespread application of new microstructural studies (EBSD), combined with other multidisciplinary results, has led to a study of the structural, petrological, and geophysical aspects of continental slab exhumation The physical mechanism and reentry mode have a deeper understanding [25]. A large number of examples show that many deformation images and deformation laws observed in the microscopic field (such as pressure shadow, multiple fracture closure mechanism of rock deformation, deformation decomposition, etc.) can be applied to the macroscopic structural analysis, which is also a supplement to the field structural geological work methods.

3. Results and Discussion

3.1. Various Mineral Petrological and Geochemical Analysis Methods. The samples were tested in this paper using a variety of mineral petrological and geochemical analysis methods [26]. There is a traditional whole rock major element analysis, electron probe (EMP) mineral in situ major element analysis, scanning electron microscope (SEM) element surface scanning analysis, cathodoluminescence (CL), and backscattering (BSE) structural analysis of limestone, etc [27]. There are also emerging in situ laser Raman spectroscopy analysis, laser ablation single mineral in situ major and quantitative element analysis, zircon in situ U-Pb dating and trace element analysis, zircon in situ Lu-Hf isotope analysis, etc. analytical skills [28]. The effective combination of the two can increase the spatial resolution of the correlation analysis to a range of several to hundred meters. Many problems are difficult to solve by traditional methods. Since in situ Lu-Hf isotope analysis of zircon is often used in current analysis, the following mainly introduces the in situ Lu-Hf isotope analysis of zircon [29–33].

The zircon Lu-Hf isotopic analysis in this paper was carried out in two batches. One batch was completed in the State Key Laboratory of Continental Dynamics, Northwestern University, using GeoLas2005 193 nm excimer laser, Nu Plasma HR type MC-ICPMS and Varian 820-MS type Q-ICPMS. The detailed analytical procedure and instrument parameters can be found in Yuan et al. In the experiment, it was used as the carrier gas, and the samples ablated by the laser were sent to Q-ICPMS and MC-ICPMS through a three-way valve to determine the Lu-Hf isotope ratio of zircon U-Pb age, respectively. The laser ablation radius is generally 44 yum. Another batch was performed at LA-MC-ICPMS, State Key Laboratory of Lithospheric Evolution, Institute of Geology and Geophysics, Chinese Academy of Sciences [34]. GeoLas 193 nm excimer laser sampling system and Neptune multireceiver inductively coupled plasma mass spectrometer were used. For a detailed analysis procedure, see Wu et al. In order to obtain an accurate 176Hf/177 ratio, an exact subtraction of 176Hf's two isotopes, 176Lu and 176Yb, must be performed. The interference of 176Yb and 176Lu is usually subtracted by the following equation (Chu et al. and Wu et al.):

$$^{176}\mathrm{Hf} = {}^{176}\mathrm{Hf}_{\mathrm{m}} - \left[{}^{175}\mathrm{Lu}_{\mathrm{m}} \times \left(\frac{^{176}\mathrm{Lu}}{^{175}\mathrm{Lu}}\right)_t \left(\frac{\mathrm{M}_{176}}{\mathrm{M}_{175}}\right)^{\beta(\mathrm{Lu})} + {}^{172}\mathrm{Yb}_{\mathrm{m}} \times \left(\frac{^{176}\mathrm{Yb}}{^{172}\mathrm{Yb}}\right)_t \left(\frac{\mathrm{M}_{176}}{\mathrm{M}_{172}}\right)^{\beta(\mathrm{Lu})} \right]. \tag{1}$$

In the formula, m is the test value, and t is the theoretical value.

There will be extrusion between zircon. In order to understand the development of the rock and the elastic wave velocity in multiple directions, the following formulas are calculated:

$$V = a(\ln P)^2 + b \ln P + c(P \leqslant P_c),$$
$$V = V_0 + DP(P \geqslant P_c),$$
$$V' = \begin{cases} \dfrac{(2a \ln P + b)}{\mathrm{P}} & (P \leqslant P_c) \\ D & (P \geqslant P_c) \end{cases}, \tag{2}$$
$$\frac{(2a \ln P_c + b)}{P_c} = D_{\circ}.$$

Since 176Lu/177Hf in zircon is usually <0.002, the interference to 176HIf mainly comes from 176Yb. In this paper, the interference of 176Lu and 176Yb was calculated by measuring the interference-free 175Lu and 172Yb according to 176Lu/175Hf = 0.02655 (Machado and Simonetti), 176Yb/172Yb = 0.887 (Wu et al.) and a correction factor. The

quality discrimination factor β was taken from the average value of β at each analysis point during the laser ablation process (Wu et al.).

The sample initial f isotope and depleted mantle model ages were calculated using the following formulas:

$$\varepsilon_{Hf}(t) = \left\{ \left[\left(\frac{^{176}Hf}{^{177}Hf} \right)_s - \left(\frac{^{176}Lu}{^{177}Hf} \right)_s \times \left(e^{\lambda t} - 1 \right) \right] / \left[\left(\frac{^{176}Hf}{^{177}Hf} \right)_{CHUR} - \left(\frac{^{176}Lu}{^{177}Hf} \right)_{CHUR} \times \left(e^{\lambda t} - 1 \right) \right] - 1 \right\} \times 10000, \tag{3}$$

$$T_{DM1} = \frac{1}{\lambda} \times \ln \left\{ 1 + \left[\left(\frac{^{176}Hf}{^{177}Hf} \right)_s - \left(\frac{^{176}Hf}{^{177}Hf} \right)_{DM} \right] / \left[\left(\frac{^{176}Lu}{^{177}Hf} \right)_s - \left(\frac{^{176}Lu}{^{177}Hf} \right)_{DM} \right] \right\}, \tag{4}$$

$$T_{DM2} = T_{DM1} - (T_{DM1} - t) \times \frac{(f_{cc} - f_s)}{(f_{cc} - f_{DM})}, \tag{5}$$

$$f_{Lu/Hf} = \frac{\left(^{176}Lu/^{177}Hf \right)_s}{\left(^{176}Lu/^{177}Hf \right)_{CHUR}} - 1, \tag{6}$$

where s is the sample, and t is the original rock age of the sample. Correlation calculated value: In = 1.865 × 10 − 11 yr 1 (Scherer et al.). The current chondrite (176HfI1T'Hf) cHURo = 0.282772, 176Lu/1 T'Hf = 0.0332 (Blichert and Albarede). The current depleted mantle is 176Lu/1Hf = 0.0384 (Griffin et al.), and the average MORB value of 176Hf/1 T"Hf is 0.28325 (Nowell et al.). The average continental crust 17Lu/17Hf is 0.015 (Griffin et al.), fe = − 0.5482; fDM = 0.15663.

In the error calculation, only the measurement error of the sample is considered, and the decay constant □ error, the chondrite 176Lu/177Hf and 176Hf/177Hf deviation, the depleted mantle 176Lu/177Hf and 176Hf/177Hf deviation, the continental crust 176Lu/177Hf deviation and other systematic errors are not considered, so the error of the calculated □Hft and the age of the depleted mantle model is smaller than the actual error.

3.2. Zircon Ce^{4+}/Ce^{3+} Ratio and Relative Oxygen Fugacity. Ce exists in the form of Ce^{3+} and Ce^{4+} in nature, and in the oxidized state, Ce^{3+} in magma is easily oxidized to Ce^{4+}, while Ce^{4+} has similar ionic radius and charge number as Zr^{4+}, so Ce^{4+} is easier to replace zirconium The Zr^{4+} in the stone enters into the zircon, resulting in the positive anomaly of Ce in the zircon. As Ce^{3+} in magma is oxidized to Ce^{4+} and enters into zircon, Ce^{3+} and Ce^{4+} in zircon are differentiated. Therefore, we can characterize the relative oxygen fugacity characteristics of magma during separation and crystallization by calculating the ratio of zircon Ce^{4+}/Ce^{3+}.

The ratio of Ce^{4+}/Ce^{3+} can be calculated by the formula proposed by Ballard:

$$\left[\frac{Ce^{4+}}{Ce^{3+}} \right]_{zircon} = \frac{\left(Ce_{fusant} - Ce_{zircon} / D_{Ce^{3+}}{}^{zircon/fusant} \right)}{\left(Ce_{zircon} / D_{Ce^{4+}}{}^{zircon/fusant} - Ce_{fusant} \right)}. \tag{7}$$

The lattice strain model is the theoretical basis for all zircon oxygen fugacity meters. According to the lattice strain model, it can be known that the partition coefficient between all zircon and the melt satisfies the following formula

$$D_i = D_0 \exp \left[-\frac{4\pi \mathrm{EN}_A}{RT} \left(\frac{r_0}{2} (r_0 - r_i)^2 - \frac{1}{3} (r_0 - r_i)^3 \right) \right]. \tag{8}$$

By simplifying Formula (4), we can get:

$$\ln D_i = \ln D_0 - \frac{4\pi \mathrm{EN_A}}{\mathrm{RT}} \left(\frac{r_i}{3} + \frac{r_0}{6} \right) (r_i - r_0)^2. \tag{9}$$

3.3. Absolute Oxygen Fugacity. The zircon Ce^{4+}/Ce^{3+} ratio discussed above characterizes the relative oxygen fugacity of the rock mass. By comparing the zircon Ce^{4+}/Ce^{3+} ratio, it can indicate the relative oxygen fugacity during the formation of the rock mass. However, in order to quantitatively evaluate the mineralization potential of a rock mass, it is obviously not enough to only rely on the Ce^{4+}/Ce^{3+} ratio of cobaltite.

Trail et al. summed up the empirical formula for calculating the absolute oxygen fugacity of rock mass by calibrating the relationship between zircon Ce anomaly, temperature and oxygen fugacity:

$$\ln \left(\frac{\mathrm{Ce}}{\mathrm{Ce}^*} \right)_{\mathrm{D}} = (0.1156 \pm 0.0050) \times \ln \left(f_{\mathrm{O}_2} \right) + \frac{13860 \pm 708}{T} - 6.125 \pm 0.484. \tag{10}$$

T in the formula is the absolute temperature (K) when the zircon crystallizes, which can be obtained according to the Ti thermometer in the zircon corrected by Watson:

$$T = \frac{5080 \pm 30}{(6.01 \pm 0.03) - \log (\mathrm{Ti})}. \tag{11}$$

The new (oxygen fugacity meter) formula proposed by Smythe and Brenan is as follows:

$$\mathrm{n} \left(\frac{X^{\mathrm{melt}}_{\mathrm{Ce}^{4+}}}{X^{\mathrm{melt}}_{\mathrm{Ce}^{4+}}} \right) = \frac{1}{4} \ln \left(f_{\mathrm{O}_2} \right) + \frac{13136(\pm 591)}{T} - 2.064(\pm 0.011), \frac{\mathrm{NBO}}{T} - 8.878(\pm 0.122) \cdot x\mathrm{H_2O} - 8.955(\pm 0.091) \tag{12}$$

where T is the absolute temperature (K) of the zircon crystallizing, which can be calculated according to the Ti thermometer proposed by Ferry (Equation (8)). NBO/T is the

ratio of nonbridged oxygen to tetrahedral cations, which can be calculated by using the main elements of the whole rock. Do the calculations; xH_2O is the mole fraction of water in the melt.

4. Result Analysis and Discussion

4.1. Mineral Composition. Eclogites belong to high-pressure and medium and low-temperature metamorphic rocks in petrological classification. The surface exposure is very rare and the occurrence is very complex. They are generally in the core of the orogenic belt and often represent the boundary of the ancient plate. It can become an inclusion in kimberlite, and can also be produced in bands in garnet peridotite. Eclogite can be associated with some granulite facies rocks, and it can also be associated with blue amphibole schist in high-pressure metamorphic belt. The main and trace elements of the whole eclogite in the North Qilian Mountains are analyzed mainly for massive eclogite and schistose eclogite. Before sample analysis, the quartz vein part in massive eclogite and the quartz+garnet layer in schistoid eclogite were excised. The analysis results are shown in Figures 1 and 2. The results show that the massive eclogite and schistoid eclogite have significantly different contents of major and trace elements, but the eclogites (09WD21 and 09WD22, 09WD25 and 09WD26) within the same occurrence are not very different. The SiO_2 content of massive eclogite is about 47 wt.%, and the total alkali (K_2O and Na_2O) content is 3.09-4.17 wt.%. The flaky eclogite 09WD25 has a SiO_2 content of 55.0 wt.%, a total of KO and Na_2O of 2.64 wt.%, and 09WD26 has a SiO_2 and K_2O +Na2O of 53.4 wt.% and 3.93 wt.%, respectively, so both of them are The basaltic andesite region that falls on the silico-alkali map (Figure 1). In addition, the Fe and Ti contents in massive eclogites are significantly higher than those in flaky eclogites.

On the normalized trace element spider web map of the original mantle (Figure 2), both massive eclogites and schistocene eclogites have island arc-type trace element distribution patterns. On the whole, however, flaky eclogites contain higher LILE and HFSE than massive eclogites.

Figures 1 and 2 also list the Cheng and Jahn samples taken from the same area in the literature. It can be seen that they are basically consistent with the schistoid eclogite in whole-rock composition.

The averaged Ca and Mg values of the core and edge of the massive eclogite garnet are (0.32, 0.145) and (0.265, 0.212), respectively, which are projected on the calculated pseudoscopic section, corresponding to (573°C, 21Kbar) and (590°C, 23Kbar), respectively. Connecting these two points and simply extending linearly to 510°C and 650°C, the resulting straight lines approximately represent the metamorphic path of massive eclogite. Then, at 1°C intervals, the changes of mineral content and garnet composition along the metamorphic pathway were simulated step by step.

The garnet composition of flaky eclogite is less ideal than that of massive eclogite. The results of whole-rock simulation of flaky eclogite show that its garnet has a high Ca isoline (0.26-0.38) in the calculated temperature (500-650°C) and pressure (12-28 kbar) domains, slightly higher than the measured value of the actual sample (0.22-0.28). However, considering that the two samples (09WD22 and 09WD25) were taken from the same outcrop and were less than 4 m apart, it can be considered that the schist oscillated eclogites experienced a P-T metamorphic trajectory consistent with the massive eclogites.

Two occurrences of high-pressure eclogites on the same outcrop in the northern Qilian Mountains: massive eclogite and schistose eclogite, which are less than 4 m apart, implying that they experienced the same P-T-t path but different degree of structural deformation. At the same time, the major elements of the whole rock show obvious differences between the two, and the flaky eclogite has higher quartz and iron content and lower magnesium content. This provides an opportunity for us to comprehensively study the growth control of garnet in eclogite by whole rock composition and temperature and pressure conditions.

4.2. Oxygen Fugacity. Oxygen fugacity (fo_2) is the effective partial pressure of oxygen. Oxygen partial pressure refers to the partial pressure of oxygen under the total pressure of the mixed gas, expressed in PO_2. If the total pressure of air is regarded as an atmospheric pressure, and the main composition of air is O_2 accounting for about 21% of the volume and N_2 accounting for about 79% of the volume, their partial pressure is po2 = 0.21 atm, n2 = 0.79 atm. For ideal gases, oxygen fugacity is the partial pressure of oxygen. For real gas, oxygen fugacity is the corrected effective oxygen partial pressure. According to the samples taken from the Qilian Mountains, the standardized distribution patterns of zircon and whole-rock trace element chondrites of the sample rock mass were drawn (Figures 3, 4, 5).

From the Th/U ratio of each rock mass, it can be seen that the zircon in the rock mass are all typical magmatic zircon (Th/U >0.5). From Figures 3 and 4, it can be seen that the zircon rare earth element distribution map of foliated and massive eclogite shows a strong left-leaning trend. The fractionation of light and heavy rare earths in zircon is obvious, which is strongly enriched in heavy rare earths, depleted in light rare earths, and has Eu. Negative anomalies and obvious positive Ce anomalies; the zircon rare earth element distribution map of the rock mass without ore also has a slight left-leaning trend, the light rare earths are relatively depleted, and the heavy rare earths are gradually enriched, with a negative anomaly of Eu and no Ce anomaly. The positive anomaly of Ce in zircon is caused by Ce^{4+} replacing Zr^{4+} in zircon and entering zircon; under relative oxidation conditions, Ce^{3+} is oxidized to Ce^{4+} in large quantities, which will lead to an increase in the positive anomaly of Ce in zircon. In the process of magma crystallization and differentiation, a large amount of Eu2+ enters plagioclase, which leads to the negative anomaly of Eu in zircon; while Eu^{3+} is incompatible with plagioclase, so with the increase of oxygen fugacity, Eu^{2+} is oxidized to Eu^{3+}, Eu anomaly in zircon is reduced. Compared with the zircon of the ore-free rock mass, the zircon of the ore-bearing rock mass has an obvious positive Ce anomaly and a lower Eu negative anomaly, indicating that the ore-bearing rock mass has a relatively higher oxygen fugacity.

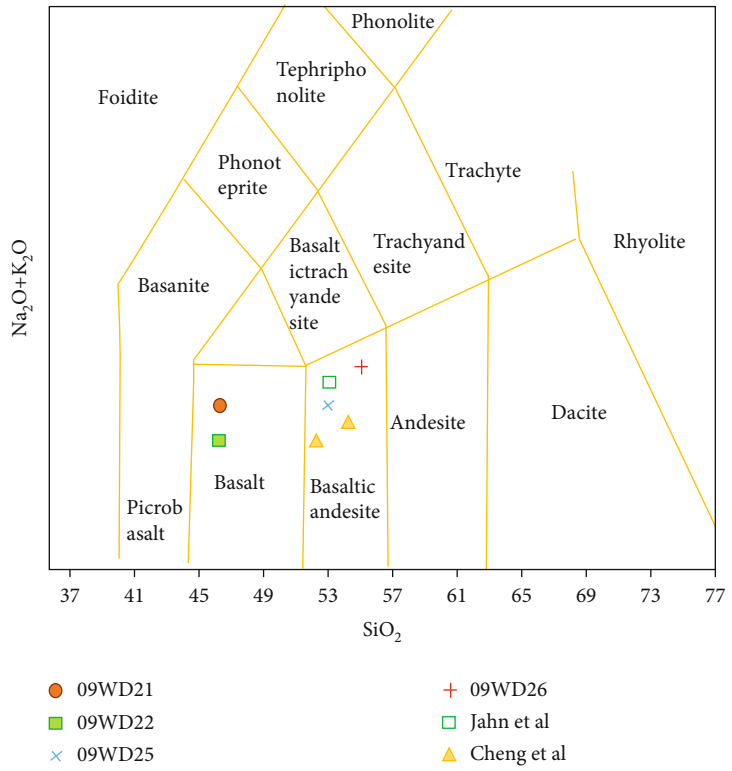

Figure 1: Diagram of the main element silico-alkali.

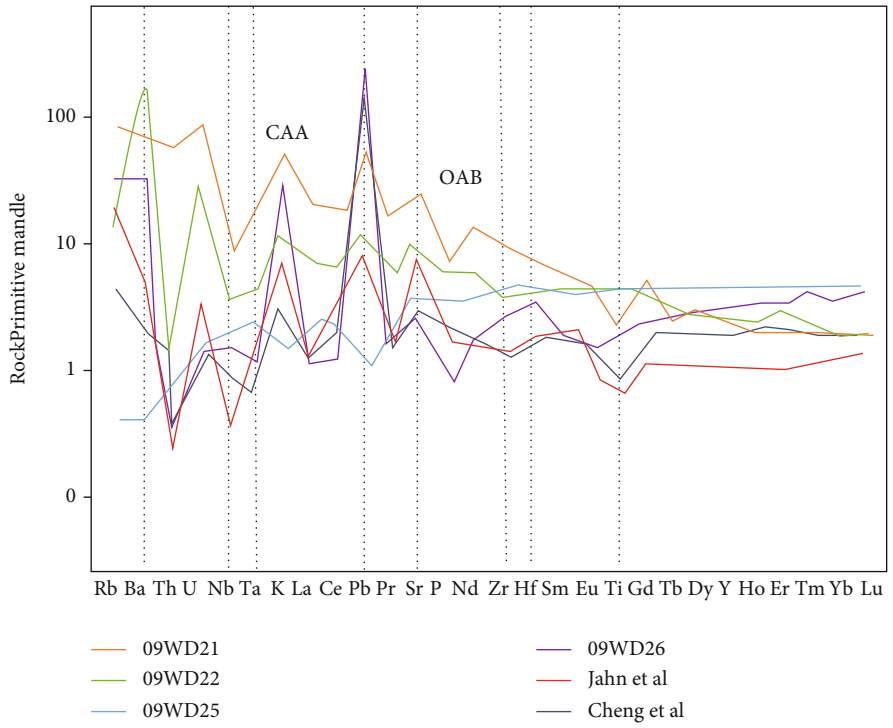

Figure 2: Cobweb diagram of trace elements normalized in the primitive mantle.

From the whole-rock rare earth element distribution pattern (Figure 5), it can be seen that the change trend and characteristics of rare earth elements in ore-bearing and non-ore-bearing rock bodies are basically the same, and they all show a right-dipping trend. The fractionation of light and heavy rare earths is obvious, and the light rare earths are relatively enriched while there is loss of heavy rare earths.

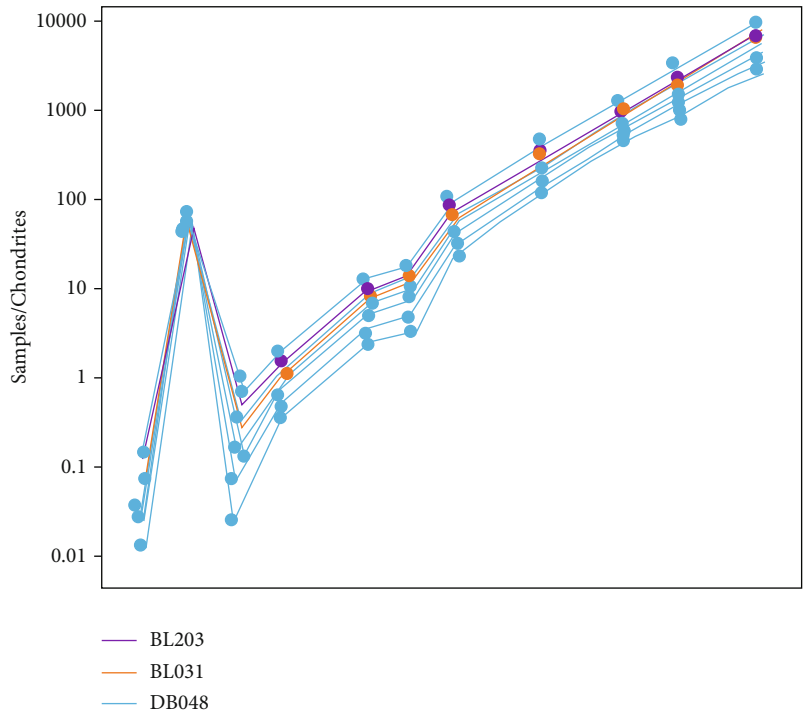

Figure 3: Normalized partition pattern of physicochemical eclogite zircon chondrites.

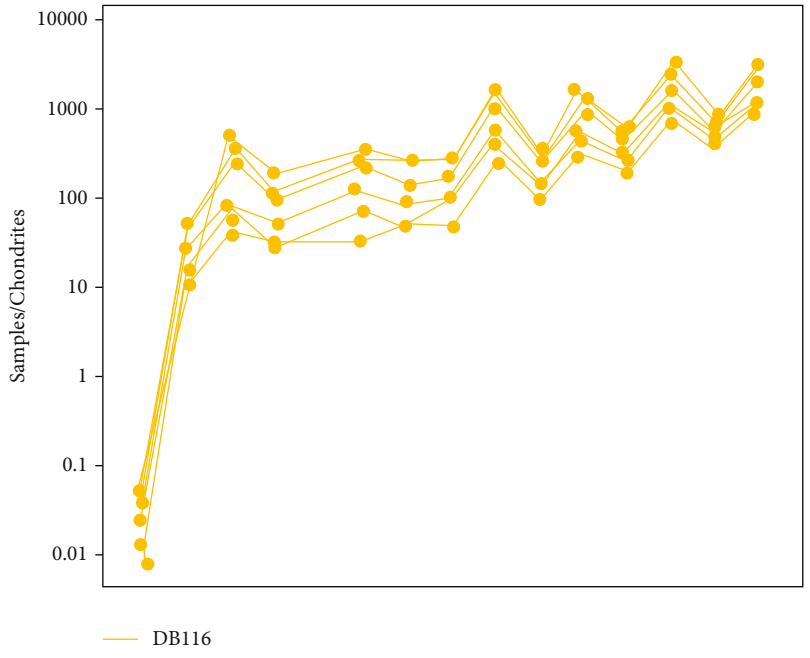

Figure 4: Normalized partition pattern of massive eclogite zircon chondrites.

The specific solution process has been introduced in great detail by Ballard and Xin, and will not be repeated in this article. So far, the four values for solving the Ce^{4+}/Ce^{3+} ratio in zircon have been obtained. Putting them into Formula (7) can solve the Ce^{4+}/Ce^{3+} ratio in the zircon of each sample rock mass.

The result in Figure 6 shows that the zircon Ce^{4+}/Ce^{3+} ratios of the ore-bearing granodiorite porphyry (BL023, BL031) in the faceted eclogite deposit are 536.03 and 492.18, respectively. The ratio of zircon Ce^{4+}/Ce^{3+} is 454.02, and the zircon Ce^{4+}/Ce^{3+} ratio of granodiorite porphyry (DB116) is 0.67. In addition, the calculated zircon

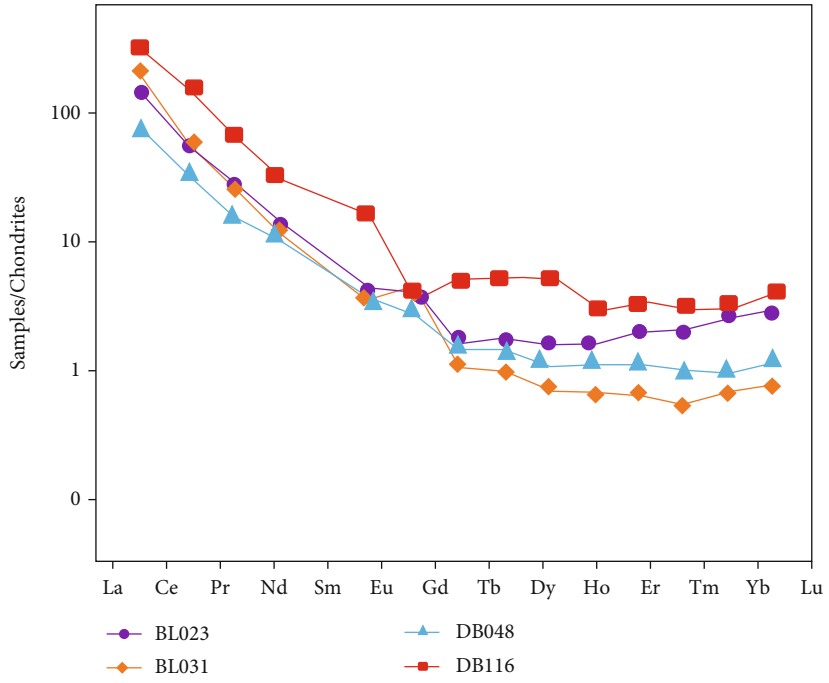

Figure 5: Normalized distribution pattern of rare earth element chondrites.

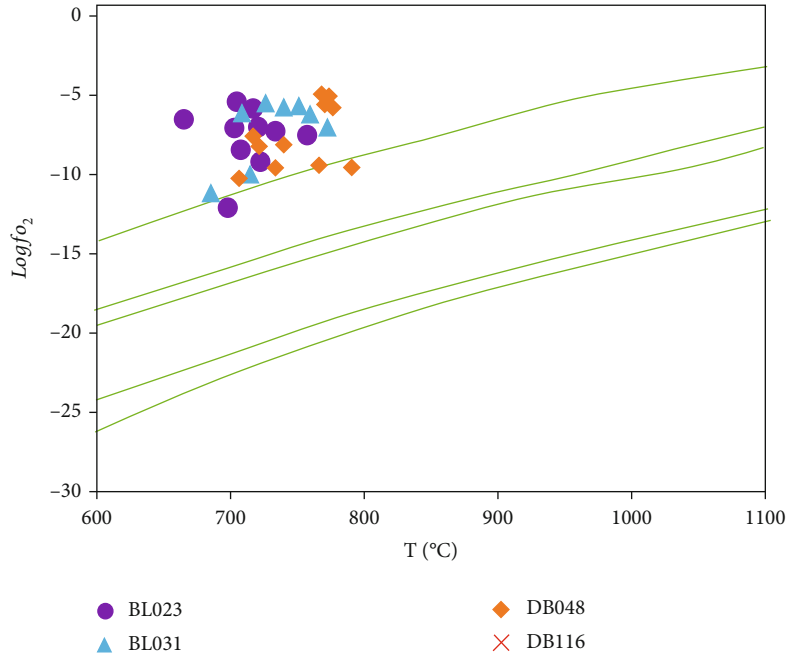

Figure 6: Physical and chemical oxygen fugacity log(fo_2) of eclogite deposits.

Ce^{4+}/Ce^{3+} ratio of each rock mass was projected, and it was concluded that the zircon Ce^{4+}/Ce^{3+} ratio of the ore-bearing porphyry body of the faceted and massive deposit was significantly higher than that of the ore-free porphyry body. This indicates that the ore-bearing porphyry bodies were formed in a relatively higher oxygen fugacity environment.

The result as shown in Figure 7 shows that the oxygen fugacity of the ore-bearing granodiorite porphyries (BL023, BLO31, DB048) in both the surface and massive eclogite deposits are all located above the MH (magnetite-hematite) buffer zone, with an average △MH+4.04, AMH+384 and ΔMH+1.85. The oxygen fugacity distribution of the ore-free granodiorite porphyry (DB116) is relatively scattered, and it is basically located near the FMQ (fayalite-magnetite-quartz), with an average value of △FMQ+0.72. It can also be seen from the calculation results of the absolute

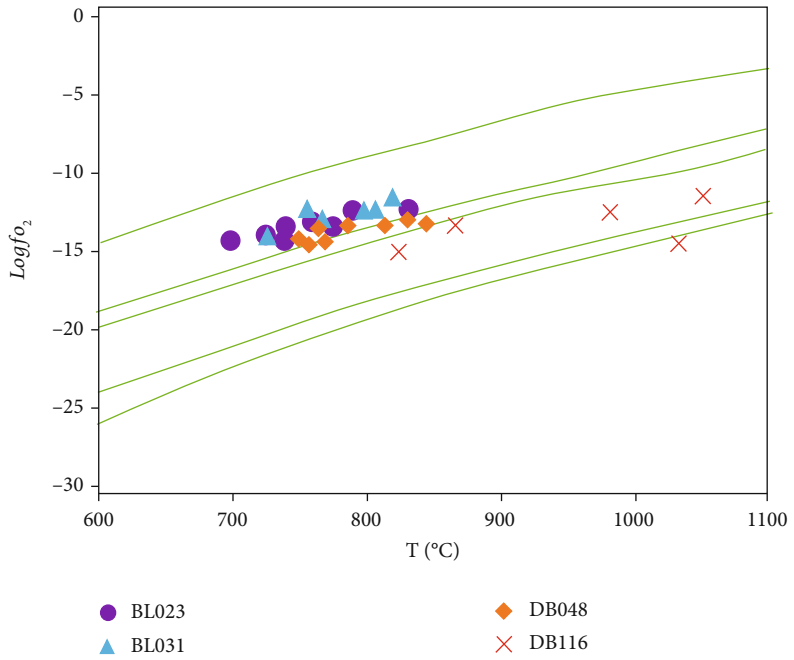

Figure 7: Oxygen fugacity log(fo_2) of massive eclogite deposits.

oxygen fugacity of the rock mass that the absolute oxygen fugacity of the ore-bearing rock mass is significantly higher than that of the ore-free rock mass.

5. Conclusion

Based on the petrology, structure and geophysics of massive and foliated eclogites in the North Qilian orogenic belt, and the changes in mineral composition, oxygen fugacity and fabric during the exhumation process, the following conclusions are drawn According to the characteristics of fabric changes, the mineral generations of massive and foliated eclogites in the North Qilian orogenic belt can be divided into: the first-generation mineral assemblage: ommatite, rutile and epidote inclusions in garnet, represents the subduction into the metamorphic stage. The second-generation mineral assemblage: including garnet, omphacite, muscovite and rutile, representing the peak metamorphic assemblage of high-pressure eclogite facies. The third-generation mineral assemblage is mainly composed of garnet retrograde edges such as diopside, albite, quartz, amphibole and post-synthetic crystals of ommatite, representing the retrograde stage of amphibole facies. The fourth-generation mineral assemblage: mainly composed of chlorite, quartz and biotite in the mineral edges and fissures, representing the retrograde stage of greenschist facies.

Data Availability

The figures used to support the findings of this study are included in the article.

Conflicts of Interest

The authors declare that they have no conflicts of interest.

Acknowledgments

This work was supported by the Basic Geological Survey of Shale Gas in south Jiangsu and Anhui, China (Grant No. DD20190083). The authors would like to show sincere gratitude to those who have contributed to this research.

References

[1] R. Tao, L. Zhang, M. Tian et al., "Formation of abiotic hydrocarbon from reduction of carbonate in subduction zones: constraints from petrological observation and experimental simulation," *Geochimica et Cosmochimica Acta*, vol. 239, pp. 390–408, 2018.

[2] S. Guo, P. Tang, B. Su et al., "Unusual replacement of Fe-Ti oxides by rutile during retrogression in amphibolite-hosted veins (Dabie UHP terrane): a mineralogical record of fluid-induced oxidation processes in exhumed UHP slabs," *American Mineralogist*, vol. 102, no. 11, pp. 2268–2283, 2017.

[3] Y. Zhang, C. Wei, and H. Chu, "Multi-phase metamorphism in the northern margin of the North China craton: records from metapelite in the Hongqiyingzi complex," *Gondwana Research*, vol. 98, pp. 289–308, 2021.

[4] Y. Ren, D. Chen, D. E. Kelsey, X. Gong, and L. Liu, "Petrology and geochemistry of the lawsonite (pseudomorph)-bearing eclogite in Yuka terrane, north Qaidam UHPM belt: an eclogite facies metamorphosed oceanic slice," *Gondwana Research*, vol. 42, pp. 220–242, 2017.

[5] Z. Li, Y. Li, J. R. Wijbrans, Q. Yang, H. N. Qiu, and F. M. Brouwer, "Metamorphic P-T path differences between the two UHP terranes of Sulu Orogen, eastern China: petrologic comparison between eclogites from Donghai and Rongcheng," *Journal of Earth Science*, vol. 29, no. 5, pp. 1151–1166, 2018.

[6] H. Yuan, J. Wang, and K. Hattori, "Ultrahigh-pressure metamorphism and P-T path of Xiaoxinzhuang Eclogites from the southern Sulu Orogenic Belt, eastern China, Based on

Phase Equilibria Modelling," *Minerals*, vol. 12, no. 2, p. 216, 2022.

[7] Y. Cao, J. Du, H. Jung et al., "Crystal preferred orientations, deformation mechanisms and seismic properties of high pressure metamorphic rocks from the Central Qiangtang metamorphic belt, Tibetan Plateau," *Journal of Structural Geology*, vol. 145, article 104309, 2021.

[8] A. Dey, K. Sen, M. A. Mamtani, and F. McCubbin, "Electron backscatter diffraction study of ultrahigh-pressure Tso Morari eclogites (Trans-Himalayan Collisional Zone): implications for strain regime transition from constrictional to plane strain during exhumation," *Lithosphere*, vol. 2022, no. 1, 2022.

[9] X. Li, "Microprobe analysis of ferric iron in garnet: the flank method and case application," *Acta Petrologica Sinica*, vol. 35, no. 4, pp. 1058–1070, 2019.

[10] R. Negrete-Aranda, E. Ca?ón-Tapia, J L. Brandle, M A. Ortega-Rivera, J K W. Lee, and R M. Spelz, "Regional orientation of tectonic stress and the stress expressed by post-subduction high-magnesium volcanism in northern baja california, mexico: tectonics and volcanism of san borja volcanic field," *Journal of Volcanology & Geothermal Research*, vol. 1-2, no. 192, pp. 97–115, 2010.

[11] X. Chen, H. P. Schertl, E. Hart et al., "Mobilization and fractionation of Ti-Nb-Ta during exhumation of deeply subducted continental crust," *Geochimica et Cosmochimica Acta*, vol. 319, pp. 271–295, 2022.

[12] K. F. Fornash, D. L. Whitney, and N. C. A. Seaton, "Lawsonite composition and zoning as an archive of metamorphic processes in subduction zones," *Geosphere*, vol. 15, no. 1, pp. 24–46, 2019.

[13] J. Lee and H. Jung, "Lattice-preferred orientation and seismic anisotropy of minerals in retrograded eclogites from Xitieshan, northwestern China, and implications for seismic reflectance of rocks in the subduction zone," *Minerals*, vol. 11, no. 4, p. 380, 2021.

[14] S. Sun, Y. Dong, X. Liu, D. He, and C. Cheng, "Fabrics, geothermometry, and geochronology of the Songshugou ophiolite: insights into the tectonic evolution of the Shangdan suture, Qinling Orogen, China," *Lithosphere*, vol. 11, no. 6, pp. 784–803, 2019.

[15] W. Liu, H. Xu, and F. Shi, "Decorated dislocations in naturally deformed olivine with c-type fabric: a case study in the Luliangshan garnet peridotite from the North Qaidam ultrahigh-pressure belt, NW China," *Tectonophysics*, vol. 814, article 228971, 2021.

[16] Y. Cao, X. Guo, and J. Du, "Electrical conductivity of eclogite, amphibolite and garnet-quartz-mica schist with implications for the conductivity in the Qiangtang terrane of northern Tibetan Plateau," *Journal of Earth Science*, vol. 31, no. 4, pp. 683–692, 2020.

[17] H. Yu, H. F. Zhang, and M. Santosh, "Mylonitized peridotites of Songshugou in the Qinling Orogen, Central China: a fragment of fossil oceanic lithosphere mantle," *Gondwana Research*, vol. 52, pp. 1–17, 2017.

[18] P. Tang and S. Guo, "Epidote records subduction-zone metamorphic fluid actions," *Acta Petrologica Sinica*, vol. 35, no. 7, pp. 2045–2060, 2019.

[19] H. Jung, "Crystal preferred orientations of olivine, orthopyroxene, serpentine, chlorite, and amphibole, and implications for seismic anisotropy in subduction zones: a review," *Geosciences Journal*, vol. 21, no. 6, pp. 985–1011, 2017.

[20] J. Wei, H. Cheng, B. Fan, Z. Tan, L. Tao, and L. Ma, "Research and practice of" one opening-one closing" productivity testing technology for deep water high permeability gas wells in South China Sea," *Fresenius Environmental Bulletin*, vol. 29, no. 10, pp. 9438–9445, 2020.

[21] J. Han, H. Cheng, Y. Shi, L. Wang, Y. Song, and W. Zhnag, "Connectivity analysis and application of fracture cave carbonate reservoir in Tazhong," *Science Technology and Engineering*, vol. 16, no. 5, pp. 147–152, 2016.

[22] X. Wei, Y. Guo, H. Cheng et al., "Rock mass characteristics in Beishan, a preselected area for China's high-level radioactive waste disposal," *Acta Geologica Sinica*, vol. 93, no. 2, pp. 362–372, 2019.

[23] L. Yang, S. Song, M. B. Allen, L. Su, J. Dong, and C. Wang, "Oceanic accretionary belt in the west Qinling Orogen: links between the Qinling and Qilian Orogens, China," *Gondwana Research*, vol. 64, pp. 137–162, 2018.

[24] F. Yuan, J. Liu, E. J. M. Carranza et al., "The Guangshigou uranium deposit, northern Qinling Orogen, China: a product of assimilation-fractional crystallization of pegmatitic magma," *Ore Geology Reviews*, vol. 99, pp. 17–41, 2018.

[25] J. Soldner, C. Yuan, K. Schulmann et al., "Early paleozoic cascadia-type active-margin evolution of the Dunhuang block (NW China): geochemical and geochronological constraints," *GSA Bulletin*, vol. 134, no. 9-10, pp. 2503–2530, 2022.

[26] S. Yang, G. Yang, W. Qu et al., "Pt-Os isotopic constraints on the age of hydrothermal overprinting on the Jinchuan Ni-cu-PGE deposit, China," *Mineralium Deposita*, vol. 53, no. 6, pp. 757–774, 2018.

[27] H. Q. Xing, X. W. Li, J. F. Xu et al., "The genesis of felsic magmatism during the closure of the Northeastern Paleo- Tethys Ocean: evidence from the Heri batholith in West Qinling, China," *Gondwana Research*, vol. 84, pp. 38–51, 2020.

[28] K. A. Evans and A. G. Tomkins, "Redox variables and mechanisms in subduction magmatism and volcanism," in *Magma Redox Geochemistry*, pp. 63–91, American Geophysical Union (AGU), 2021.

[29] H. Jung, "Erratum to: crystal preferred orientations of olivine, orthopyroxene, serpentine, chlorite, and amphibole, and implications for seismic anisotropy in subduction zones: a review," *Geosciences Journal*, vol. 22, no. 3, pp. 523–550, 2018.

[30] P. Gao, Y. H. Lu, Z. F. Zhao, and Y. F. Zheng, "The compositional variation of I-type granites: constraints from geochemical analyses and phase equilibrium calculations for granites from the Qinling Orogen, Central China," *Journal of Asian Earth Sciences*, vol. 200, article 104471, 2020.

[31] Z. Zhao, J. Wei, S. Liang, and T. Gao, "Sulfide remobilization and trace element redistribution during metamorphism and deformation at the Xitieshan Pb-Zn deposit, NW China," *Ore Geology Reviews*, vol. 136, article 104170, 2021.

[32] G. Yang, Y. Li, L. Tong, Z. Wang, and L. Wu, "Oceanic Island basalts in ophiolitic mélanges of the Central China Orogen: an overview," *Geological Journal*, vol. 52, pp. 155–173, 2017.

[33] X. Xiong, L. Zhu, G. Zhang et al., "Petrogenesis and tectonic implications of Indosinian granitoids from Western Qinling Orogen, China: products of magma-mixing and fractionation," *Geoscience Frontiers*, vol. 11, no. 4, pp. 1305–1321, 2020.

[34] Z. K. Hou, H. L. Cheng, S. W. Sun, J. Chen, D. Q. Qi, and Z. B. Liu, "Crack propagation and hydraulic fracturing in different lithologies," *Applied Geophysics*, vol. 16, no. 2, pp. 243–251, 2019.